



# B-Doped Carbon Powder Synthesized from PU/PF/GO Composite as Electrode Material for Supercapacitors

ZITONG LIN,<sup>1</sup> XIAOYU REN,<sup>1</sup> JINBAO LIU,<sup>1</sup> YAN SUI,<sup>1</sup>  
CHUANLI QIN,<sup>1</sup> and XIANKAI JIANG <sup>1,2</sup>

1.—School of Chemistry and Material Science, Heilongjiang University, Harbin, China.  
2.—e-mail: jiangxiankai@hlju.edu.cn

Graphite is a vital natural mineral material that is used to synthesize graphene oxide. In the present study, polyurethane/phenolic/graphene oxide composite materials were prepared from polyisocyanate prepolymer, phenolic resin prepolymer, and graphene oxide then treated with boric acid, ferric chloride, and zinc chloride and carbonized at high temperatures to synthesize boron-doped carbon powder (UFGC-B-Fe-Zn). The UFGC-B-Fe-Zn exhibited a Brunauer–Emmett–Teller specific surface area  $S_{\text{BET}}$  of  $885.9759 \text{ m}^2 \text{ g}^{-1}$  and a specific pore volume of  $0.550491 \text{ cm}^3 \text{ g}^{-1}$ , as well as high specific capacitance of  $377.4 \text{ F g}^{-1}$  at  $0.5 \text{ A g}^{-1}$ . Used as an electrode material for supercapacitors, UFGC-B-Fe-Zn exhibited excellent rate capability and durability as well as low charge and ion diffusion resistance. In 6 M KOH electrolyte, the assembled symmetrical supercapacitor achieved relatively high energy density of  $7.43 \text{ Wh kg}^{-1}$  at  $474 \text{ W kg}^{-1}$ . Moreover, it displayed excellent cycling stability (90.9% retention rate after 5000 cycles).

## INTRODUCTION

To decrease dependence on fossil fuels and reduce  $\text{CO}_2$  emissions, clean and renewable energy storage technologies are considered to represent a huge challenge.<sup>1</sup> Thus, the development of various energy storage devices capable of storing/releasing energy efficiently is imperative.<sup>2</sup> Lithium-ion batteries (LIBs) and supercapacitors (SCs) are currently considered to be the two dominant energy storage devices.<sup>3</sup> Compared with LIBs, SCs exhibit higher power density, shorter charge–discharge times, longer lifespan, and more significant environmentally friendly nature,<sup>4–6</sup> enabling their efficient application in various fields (e.g., automotive industry, electronics, and energy recovery).<sup>7</sup>

In terms of the charge storage mechanism employed, SCs can primarily be distinguished into electrical double-layer capacitors (EDLCs) and pseudocapacitors.<sup>8</sup> EDLCs achieve electrostatic storage by exploiting a potential difference to reversibly adsorb ions onto the surfaces of active electrode materials.<sup>9</sup> Meanwhile, pseudocapacitors

rely on a Faradic redox reaction.<sup>10</sup> Carbon materials such as graphene, carbon nanotubes, and carbon fibers are considered to represent ideal electrode materials for supercapacitors<sup>11,12</sup> as they exhibit high specific surface area, higher power density, thermal and chemical stability, and variable porous structure that facilitate the transport of electrolyte ions.<sup>13–16</sup> However, carbon materials display relatively low capacitance. An effective solution to address this deficiency is to introduce heteroatoms (B, P, S, N, etc.) into the carbon skeleton.<sup>17,18</sup> Such heteroatom doping can enhance the wettability of carbon materials as well as generate active sites, between which the electrolyte ions can undergo a Faraday redox reaction to improve the pseudocapacitance.<sup>19–23</sup> The specific surface area and pore structure are generally considered to be crucial features determining the electrochemical performance of materials.<sup>24</sup> Another effective solution is to improve the porosity and electrochemical performance of carbon materials by using chemical activation agents such as KOH,  $\text{ZnCl}_2$ , and  $\text{H}_3\text{PO}_4$ .<sup>25,26</sup>

In comparison with other heteroatoms, boron is considered to be the best choice since it has a similar number of valence electrons and atomic size to carbon.<sup>27</sup> Boron doping can be achieved by several

(Received October 4, 2020; accepted December 28, 2020;  
published online February 3, 2021)

Table I. Pore structure parameters and morphological parameters of the samples and relative concentrations of carbon, nitrogen, oxygen, and boron

Sample	$S_{\text{BET}}^a$ ( $\text{m}^2 \text{g}^{-1}$ )	$V_{\text{total}}^b$ ( $\text{cm}^3 \text{g}^{-1}$ )	$D_{\text{avg}}^c$ (nm)	$V_{\text{mic}}^d$ ( $\text{cm}^3 \text{g}^{-1}$ )	$V_{\text{mic}}^d$ ( $\text{cm}^3 \text{g}^{-1}$ )	$V_{\text{mes+ma}}^e$ ( $\text{cm}^3 \text{g}^{-1}$ )	Content <sup>f</sup> (at.%)						C configuration (at.%)						N configuration (at.%)					
							C	N	O	B	C=C	C-N	C-O	C=O	C-B	N-6	N-5	N-Q	N-X	N-B				
UFGC	7.2041	0.023167	14.25762	0.000365	0.000365	0.031736	87.05	5.08	7.83	0	64.03	14.62	7.94	13.41	0	15.89	25.69	44.08	14.35	0				
UFGC-B	155.1675	0.215875	5.56495	0.017526	0.017526	0.148579	81.29	8.27	8.92	1.52	42.70	19.88	14.74	17.06	5.62	24.56	19.51	10.96	21.80	23.17				
UFGC-B-Fe	282.2338	0.259096	3.67207	0.102592	0.102592	0.170141	80.8	7.9	9.5	1.81	57.77	18.63	5.96	11.65	5.99	23.88	24.49	17.37	23.58	10.69				
UGFC-B-Fe-Zn	885.9759	0.550491	2.48536	0.393158	0.393158	0.331632	83.59	5.37	9.32	1.72	52.08	15.55	11.82	12.62	7.92	20.95	37.43	6.79	24.94	9.89				

Sample	$S_{\text{BET}}^a$ ( $\text{m}^2 \text{g}^{-1}$ )	$V_{\text{total}}^b$ ( $\text{cm}^3 \text{g}^{-1}$ )	$D_{\text{avg}}^c$ (nm)	$V_{\text{mic}}^d$ ( $\text{cm}^3 \text{g}^{-1}$ )	$V_{\text{mes+ma}}^e$ ( $\text{cm}^3 \text{g}^{-1}$ )	O configuration (at.%)						B configuration (at.%)					
						O-1	O-2	O-3	O-B	BC <sub>3</sub>	BC <sub>2</sub> O	B-N					
UFGC	7.2041	0.023167	14.25762	0.000365	0.031736	16.72	62.55	20.72	0	0	0	0	0	0	0	0	0
UFGC-B	155.1675	0.215875	5.56495	0.017526	0.148579	17.83	54.67	9.46	18.05	41.30	19.05	39.65	27.01	26.15	16.33	16.33	16.33
UFGC-B-Fe	282.2338	0.259096	3.67207	0.102592	0.170141	25.30	33.60	20.06	21.03	42.62	30.37	27.01	26.15	16.33	16.33	16.33	16.33
UGFC-B-Fe-Zn	885.9759	0.550491	2.48536	0.393158	0.331632	28.10	47.49	11.09	13.31	57.52	16.33	16.33	16.33	16.33	16.33	16.33	16.33

<sup>a</sup>Total specific surface area calculated by Brunauer-Emmett-Teller (BET) method<sup>b</sup>Total pore volume calculated at P/P0 = 0.99<sup>c</sup>Average pore diameter calculated from the equation of 4Vt/SBET<sup>d</sup>Micro pore volume calculated from t-Plot micropore method<sup>e</sup>Mesopore volume and macropore volume calculated from BJH method<sup>f</sup>Atomic percent of elements obtained from XPS analysis.

**Table II. Fitting values of equivalent circuit elements of the UFGC, UFGC-B, UFGC-B-Fe, and UFGC-B-Fe-Zn samples**

Equivalent circuit element	Sample			
	UFGC	UFGC-B	UFGC-B-Fe	UFGC-B-Fe-Zn
$R_S$ ( $\Omega$ )	0.67908	0.60237	0.55883	0.43897
$CPE_T$	0.0026141	0.0014585	0.0009247	0.00086857
$CPE_P$	0.78559	0.8412	0.85798	0.9126
$R_{ct}$ ( $\Omega$ )	4.474	1.262	1.095	0.75662
$W_R$	15.2	1.606	1.23	1.088
$W_T$	0.45846	0.23693	0.21376	0.18285
$W_P$	0.34336	0.31983	0.31043	0.30055

$CPE_T$  is the capacitance when  $CPE_P = 1$   $CPE_P$  is the constant-phase element exponent  $W_R$  is the diffusion resistance (Warburg diffusion resistance)  $W_T$  is the diffusion time constant  $W_P$  is a fractional exponent between 0 and 1

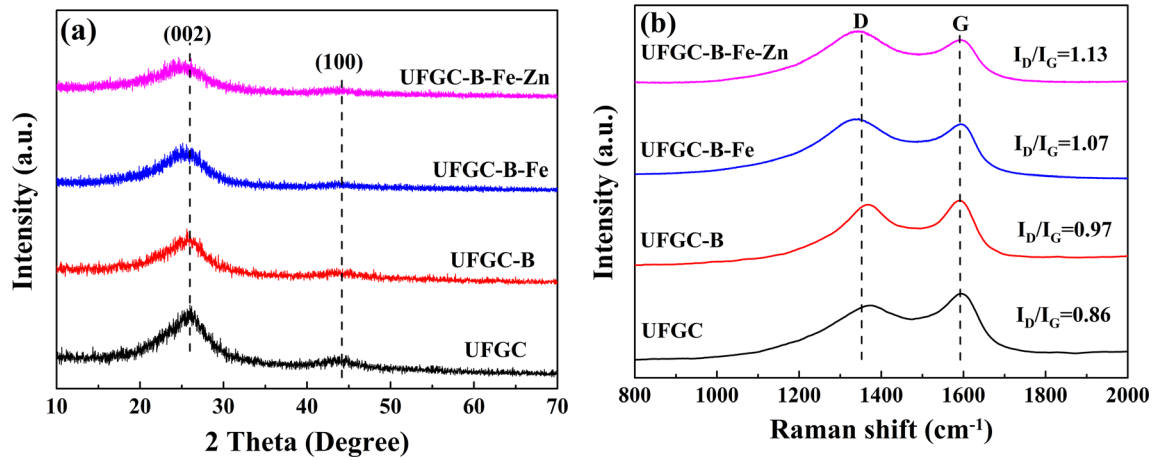


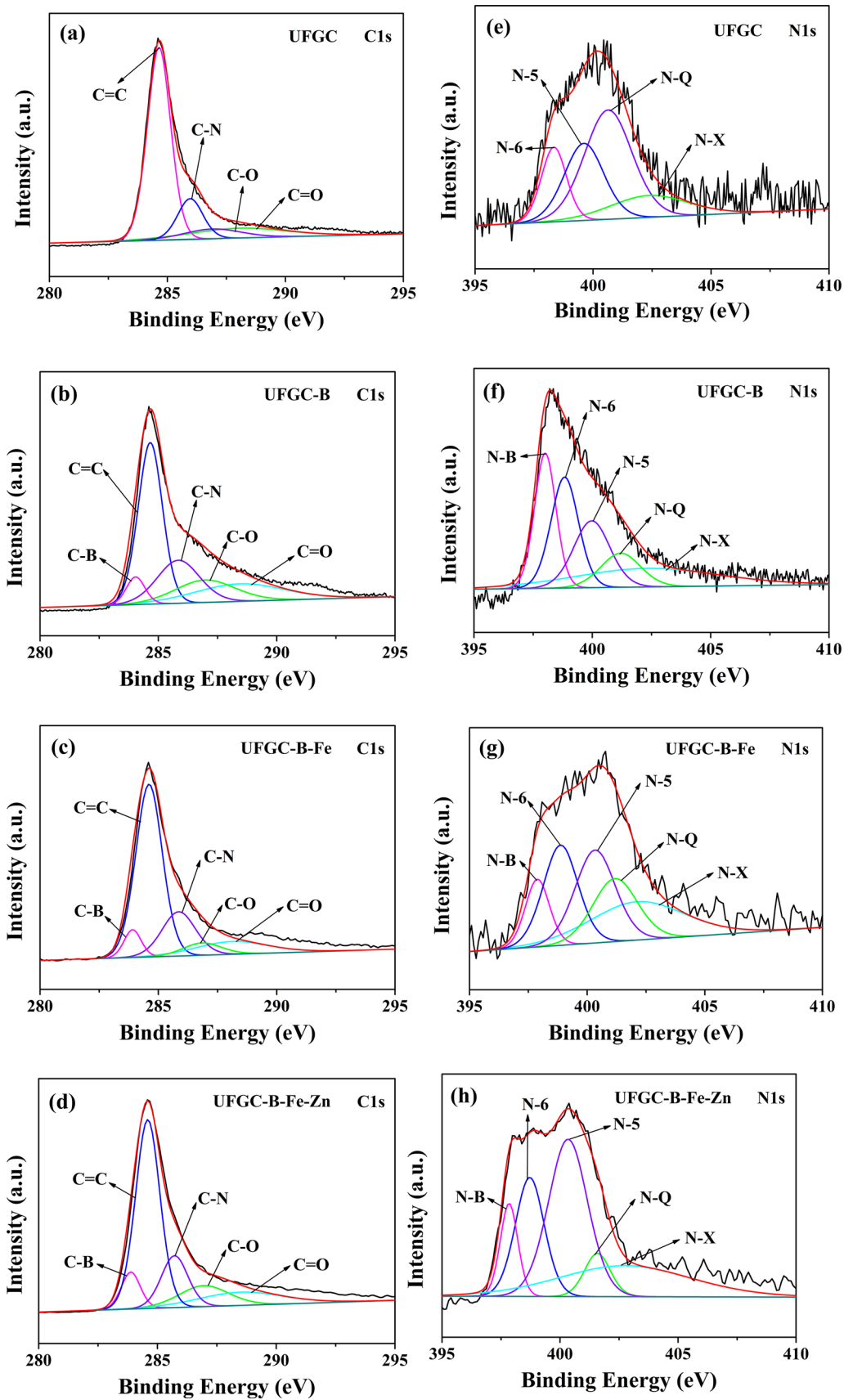
Fig. 1. (a) XRD and (b) Raman spectra of UFGC, UFGC-B, UFGC-B-Fe, and UFGC-B-Fe-Zn samples.

methods such as substitutional reaction of boron oxide ( $B_2O_3$ ), arc discharge, laser ablation, hydrothermal reaction, and chemical vapor deposition.<sup>28</sup> Li et al.<sup>29</sup> proposed a hydrothermal approach to synthesize boron-doped graphene aerogels, reporting a specific capacitance of  $308.3 \text{ F g}^{-1}$  at  $1 \text{ A g}^{-1}$ . Gao et al.<sup>30</sup> prepared ordered mesoporous carbon materials with different boron contents based on a nanometer casting method, measuring a specific capacitance of  $267.8 \text{ F g}^{-1}$  at  $5 \text{ A g}^{-1}$ . Nankya et al.<sup>31</sup> synthesized boron-doped mesoporous graphene by a hydrothermal method, achieving a specific capacitance of  $336 \text{ F g}^{-1}$  at  $0.1 \text{ A g}^{-1}$ . In Summary, boron doping of carbon materials is worth investigating in depth.

Zinc chloride ( $ZnCl_2$ ) is one of the most common agents used for chemical activation of carbonaceous materials.<sup>32</sup>  $ZnCl_2$  acts as a relatively mild chemical activator, being capable of generating pores efficaciously while avoiding hyperactivation.<sup>33</sup> During carbonization, zinc chloride can dehydrate

carbonaceous materials and aid their decomposition. Accordingly, the yield of nanoporous carbon materials synthesized using  $ZnCl_2$  activation is overall higher compared with when using other activating agents.<sup>34</sup>

Heilongjiang Province of China is significantly rich in graphite reserves. One of the raw materials used in the present study was graphene oxide synthesized from mineral graphite. Specifically, polyisocyanate prepolymer and phenolic resin prepolymer were copolymerized, then blended with graphene oxide dispersion to synthesize polyurethane/phenolic/graphene oxide (PU/PF/GO) composites. Subsequently, this was carbonized at high temperatures by doping with B atoms and activating with zinc chloride. The carbon powder material produced by pickling and water washing was used as the electrode material for supercapacitor assembly. The redox reaction of the heteroatomic functional group in the electrochemical process could be achieved through heteroatom doping to obtain



◀ Fig. 2. C 1s XPS spectra of (a) UFGC, (b) UFGC-B, (c) UFGC-B-Fe, and (d) UGGC-B-Fe-Zn. N 1s XPS spectra of (e) UFGC, (f) UFGC-B, (g) UFGC-B-Fe, and (h) UGGC-B-Fe-Zn. O 1s XPS spectra of (i) UFGC, (j) UFGC-B, (k) UFGC-B-Fe, and (l) UGGC-B-Fe-Zn. B 1s XPS spectra of (m) UFGC-B, (n) UFGC-B-Fe, and (o) UGGC-B-Fe-Zn. (p) Schematic model of N, O, and B atoms in carbon matrix. (q) XPS survey spectra of samples.

better pseudocapacitance, thereby addressing the relatively low capacitance of carbon powder materials. In addition, decreasing the content of inert B–N bonds due to the use of the ferric chloride catalyst also impacted the pseudocapacitance improvement. Removing boron oxide by water washing and activation of zinc chloride could strengthen the pore structure of the material to expand its specific surface area, thereby improving the double-layer capacitance of the carbon powder material. The supercapacitor electrode prepared using UFGC-B-Fe-Zn exhibited high specific capacitance of  $377.4 \text{ F g}^{-1}$  under current density of  $0.5 \text{ A g}^{-1}$  as well as excellent rate performance and cycling stability. The structure displayed relatively high specific surface area ( $885.9759 \text{ m}^2 \text{ g}^{-1}$ ) and pore volume ( $0.550491 \text{ cm}^3 \text{ g}^{-1}$ ). In 6 M KOH electrolyte, the manufactured symmetrical supercapacitor exhibited a prominent energy density ( $7.43 \text{ Wh kg}^{-1}$  at  $474 \text{ W kg}^{-1}$ ). Moreover, it exhibited excellent cycling stability (with a capacitance retention rate of 90.9% after 5000 cycles at  $5 \text{ A g}^{-1}$ ). The results of this investigation confirm that B-doped carbon powder can be synthesized using this simple and effective method and demonstrate that the produced material is promising for application as supercapacitor electrodes.

## EXPERIMENTAL PROCEDURES

### Preparation of PU/PF/GO Composite

Resorcinol, formaldehyde, and anhydrous sodium carbonate were mixed at molar ratio of 1:2:0.01 at  $90^\circ\text{C}$  under stirring at 300 rpm. Subsequently, deionized water was rapidly added, followed by polymerization for 4 h. The resulting solution was then vacuum dried at  $45^\circ\text{C}$  for 12 h to synthesize phenolic resin prepolymer. Graphene oxide was synthesized from natural graphite based on the Hummers method.<sup>35</sup> Trimethylolpropane and melamine were dissolved in butyl acetate at  $55^\circ\text{C}$  and stirred to form a homogeneous solution, then toluene-2,4-diisocyanate was added then reacted at  $80^\circ\text{C}$  for 4 h to produce polyisocyanate prepolymer. At  $60^\circ\text{C}$ , polyisocyanate prepolymer, phenolic resin prepolymer, graphene oxide dispersion, and dibutyltin dilaurate were mixed then stirred for 1 h to generate PU/PF/GO composite material, termed UFG.

### Preparation of Carbon Material

Employing butyl acetate as solvent, ferric chloride, boric acid, and zinc chloride were added to

UFG respectively at intervals of 1 h then stirred to mix completely. Subsequently, the solution was ultrasonically dispersed for 1 h then dried under vacuum to obtain pre-carbide. Next, the sample was transferred to a tube furnace, heated from ambient temperature to  $800^\circ\text{C}$  at a heating rate of  $5^\circ\text{C}/\text{min}$ , then carbonized under nitrogen atmosphere for 2 h. To remove iron, the sample was pickled for 48 h, then the sample was boiled at  $85^\circ\text{C}$  for 8 h to remove residual boron oxides to produce UFGC-B-Fe-Zn. Furthermore, UFGC, UFGC-B, and UFGC-B-Fe samples were generated from UFG by carbonization, followed by boric acid treatment, and without zinc chloride treatment, respectively.

### Characterization

Scanning electron microscopy (SEM, S-4800; Hitachi) was adopted to characterize the morphology of the products. X-ray diffraction (XRD) analysis (D8 ADVANCE; Bruker) was employed to determine the structure of the sample. Raman spectra were analyzed by using a Raman spectrometer (HR800; Jobin-Yvon). In addition, the chemical bonding state of the carbon materials was determined by x-ray photoelectron spectroscopy (XPS, ESCALAB 250; Thermo Fisher Scientific). Moreover, physisorption analysis (ASAP 2020 HD88; Micromeritics) was exploited to gauge the porous texture parameters of the materials under nitrogen sorption at 77 K. Furthermore, the Brunauer–Emmett–Teller (BET) method was used to determine the specific surface area. The pore size distribution of the adsorption branch was explored based on density functional theory (DFT), starting from the adsorption branch isotherm.

### Electrochemical Measurements

Cyclic voltammetry (CV), galvanostatic charge–discharge (GCD), and electrochemical impedance spectroscopy (EIS) measurements were performed at ambient temperature using a three-electrode system in an electrochemical workstation (CHI660E; Shanghai Chenhua) with 6 M KOH solution as electrolyte, and saturated calomel electrode and platinum as reference and auxiliary electrode, respectively. The material for the working electrode was a mixture of sample and polytetrafluoroethylene (at weight ratio of 95:5), uniformly mixed in ethanol then coated on nickel foam substrate ( $2 \text{ mg cm}^{-2}$ ). The CV and GCD measurements were performed over the voltage range of  $-1 \text{ V}$  to  $0 \text{ V}$  at scan rates and current densities of  $1 \text{ mV s}^{-1}$  to  $200 \text{ mV s}^{-1}$  and  $0.5 \text{ A g}^{-1}$  to  $7 \text{ A g}^{-1}$  for CV and GCD measurements, respectively. EIS tests were performed under open-circuit potential with an amplitude of  $10 \text{ V}$  in the frequency range from  $0.01 \text{ Hz}$  to  $100 \text{ kHz}$ . The specific capacitance was determined from the GCD tests by using Eq. 1.

$$C = (I \times \Delta t) / (m \times \Delta V) \quad (1)$$

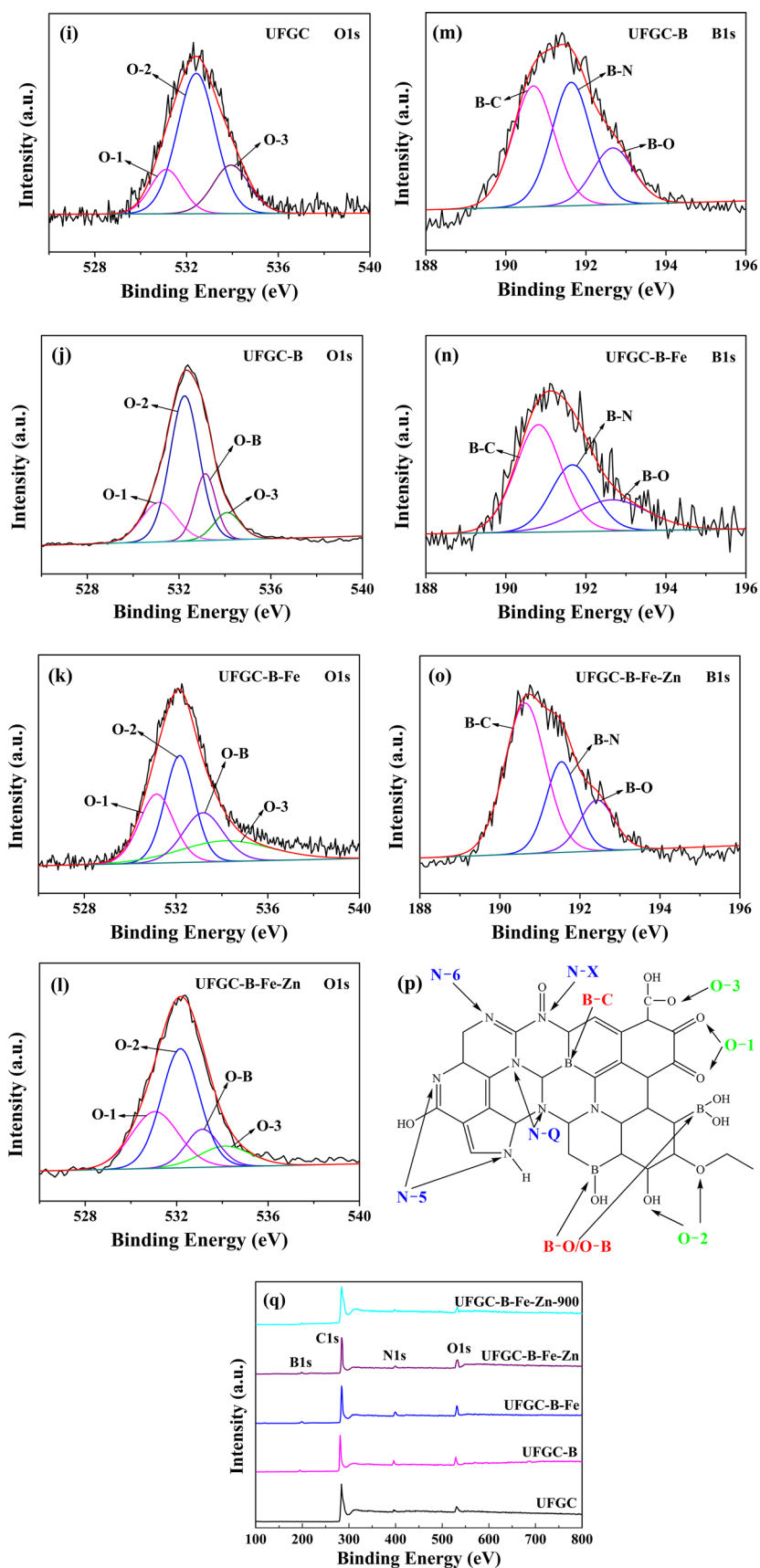


Fig. 2. continued

where  $C$  ( $F g^{-1}$ ) denotes the specific capacitance,  $I$  (A) represents the current density,  $\Delta t$  (s) is the discharge time,  $\Delta V$  (V) is the potential difference during the discharge duration, and  $m$  (g) denotes the mass of sample on the electrode.

GCD measurements were performed in a two-electrode system at current densities of  $1 A g^{-1}$ ,  $2 A g^{-1}$ ,  $3 A g^{-1}$ ,  $5 A g^{-1}$ , and  $7 A g^{-1}$ . The specific capacitance, energy density, and power density were obtained by using Eqs. 2–5:

$$C_p = (I \times \Delta t) / (m \times \Delta V) \quad (2)$$

$$C_s \approx 4C_p \quad (3)$$

$$E_p = (C_p \times \Delta V^2) / 7.2 \quad (4)$$

$$P = (3600 \times E_p) / \Delta t \quad (5)$$

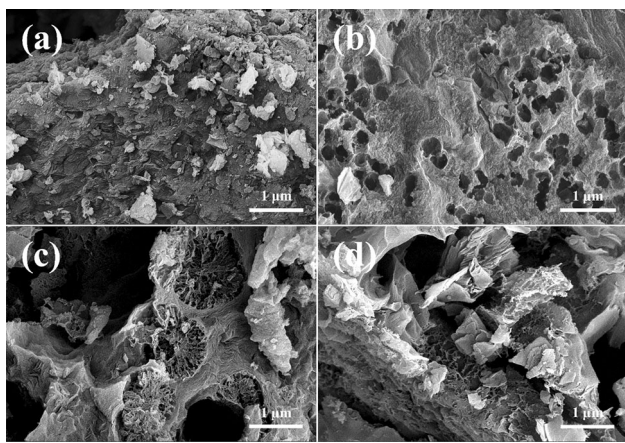


Fig. 3. SEM images showing the morphology of (a) UFGC, (b) UFGC-B, (c) UFGC-B-Fe, and (d) UFGC-B-Fe-Zn.

where  $C_p$  ( $F g^{-1}$ ),  $C_s$  ( $F g^{-1}$ ),  $E_p$  ( $Wh kg^{-1}$ ), and  $P$  ( $W kg^{-1}$ ) denote the specific capacitance, energy density, and power density, respectively.

## RESULTS AND DISCUSSION

XRD and Raman spectra were employed to compare the microstructure of the materials. The XRD spectra (Fig. 1a.) of all the samples displayed peaks at around  $26^\circ$  and  $44^\circ$ , corresponding respectively to diffraction from (002) and (001) of amorphous ordered graphite phase,<sup>36,37</sup> which suggests that addition of boric acid, ferric chloride, and zinc chloride did not effectively impact the crystalline structure of the material. Using the Bragg equation, the graphitic interlayer spacing ( $d_{002}$ ) values of UFGC, UFGC-B, UFGC-B-Fe, and UFGC-B-Fe-Zn were determined as 3.44 nm, 3.47 nm, 3.54 nm, and 3.57 nm, respectively. The (002) diffraction peak of UFGC-B-Fe-Zn was the widest, with a left shift to lower angles, suggesting the lowest graphitization degree among the samples. Moreover, UFGC-B-Fe-Zn showed the maximum  $d_{002}$ , which can probably be attributed to the introduction of heteroatoms and activation by zinc chloride that resulted in a more defective structure.

The Raman spectra (Fig. 1b) of all the samples displayed two characteristic peaks at around  $1350 cm^{-1}$  and  $1590 cm^{-1}$  corresponding to the D and G peak, respectively. The D peak corresponds to the defective and disordered portions of carbon, while the G peak corresponds to  $sp^2$ -hybridized graphitic carbon atoms.<sup>38,39</sup> The  $I_D/I_G$  ratio can be used to indirectly assess the degree of graphitization of carbon materials. UFGC, UFGC-B, UFGC-B-Fe, and UFGC-B-Fe-Zn exhibited  $I_D/I_G$  ratios of 0.86, 0.97, 1.07, and 1.13, respectively. As revealed by the higher  $I_D/I_G$  ratio of UFGC-B, treatment with boric acid resulted in a carbon material with defective structure. Specifically, the  $I_D/I_G$  ratio of UFGC-B-Fe-Zn was the maximum, indicating that activation by zinc chloride destroyed the structure

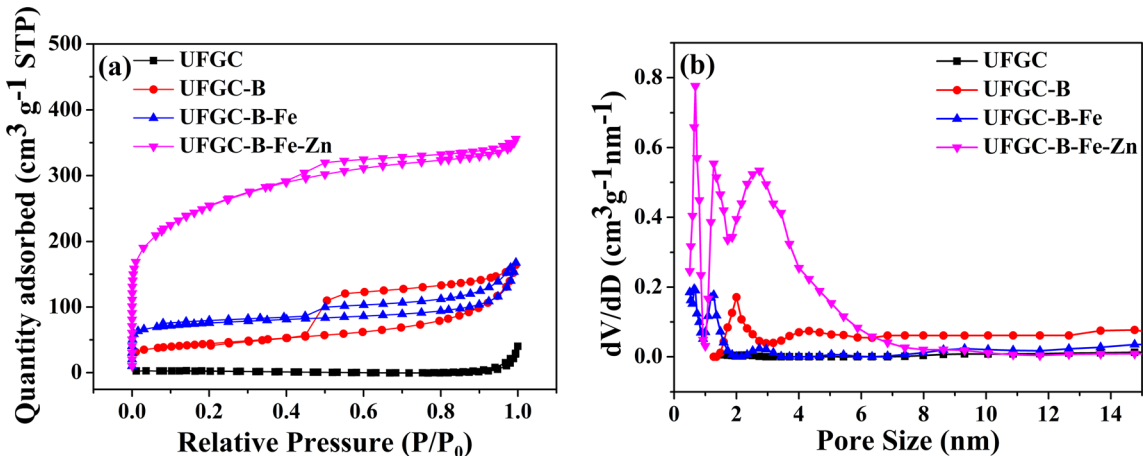
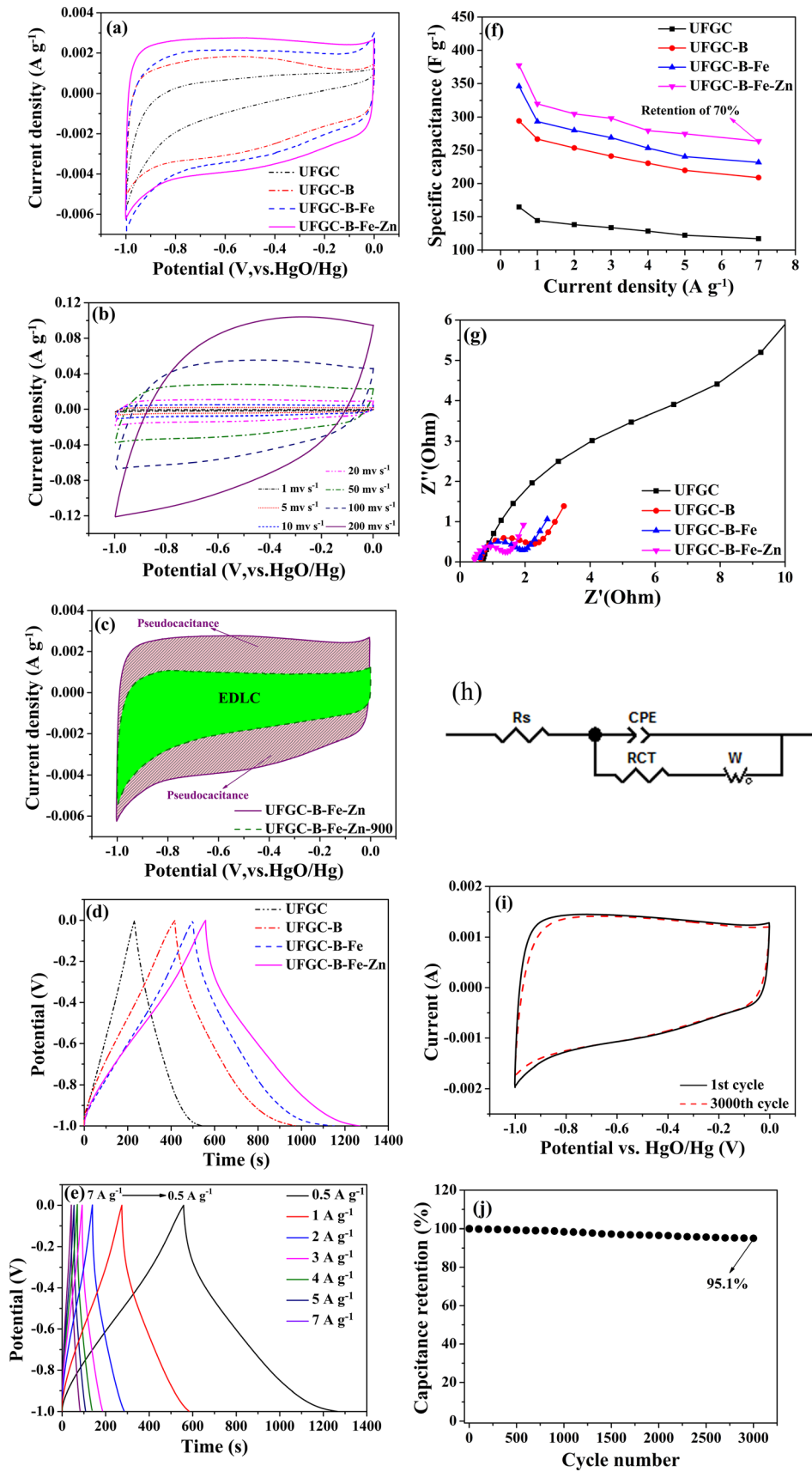


Fig. 4. (a)  $N_2$  adsorption-desorption isotherms and (b) pore size distributions of UFGC, UFGC-B, UFGC-B-Fe and UFGC-B-Fe-Zn samples.





◀Fig. 5. CV curves of (a) all samples at scan rate of  $5 \text{ mV s}^{-1}$ , (b) UFGC-B-Fe-Zn at various scan rates, and (c) UFGC-B-Fe-Zn and UFGC-B-Fe-Zn-900 at  $5 \text{ mV s}^{-1}$ . Galvanostatic charge–discharge profiles of (d) all samples at current density of  $0.5 \text{ A g}^{-1}$  and (e) UFGC-B-Fe-Zn at various current densities. (f) Specific capacitance of all samples as a function of current density at different current densities. (g) Nyquist plots of all samples. (h) Corresponding equivalent circuit model. (i) Comparison of CV curves for UFGC-B-Fe-Zn at 1st and 3000th cycles at  $20 \text{ mV s}^{-1}$ . (j) Cycling performance retention of UFGC-B-Fe-Zn.

of the material, resulting in a more defective and disordered structure with a lower degree of graphitization.

XPS was performed to determine the composition and elemental content on the sample surface. Figure 2 shows the results, while a schematic model of the heteroatoms in the carbon matrix is presented in Fig. 2p. As demonstrated by the surface elemental contents of UFGC, UFGC-B, UFGC-B-Fe, and UFGC-B-Fe-Zn (Table I), B atoms were successfully doped into the carbon skeleton structure of UFGC. Moreover, these results suggest that the contents of B, N, and O atoms in UFGC-B-Fe-Zn were reduced, which can be ascribed to partial loss of heteroatoms when the zinc chloride activation treatment formed the defective structure in the carbon material. Besides UFGC, the C 1s peaks (Fig. 2a–d) consisted of five subpeaks that can be ascribing to C–B bond (283.9 eV), C=C bond (284.6 eV), C–N bond (285.8 eV), C–O bond (286.9 eV), and C=O bond (288.4 eV), respectively.<sup>40</sup> The N 1s peaks (Fig. 2e–h) comprised five distinct components corresponding to peaks at 397.9 eV, 398.7 eV, 400.3 eV, 401 eV, and 402.3 eV belonging to N–B bond, pyridinic nitrogen (N-6), pyrrolic/pyridinic nitrogen (N-5), quaternary nitrogen (N-Q), and N-oxide group (N-X), respectively.<sup>41</sup> The O 1s spectra (Fig. 2–l) could be fit using four peaks at 531.1 eV, 532.1 eV, 533.1 eV, and 534.1 eV, derived from carboxyl functional groups (O-1), phenol groups and/or C–O–C ether groups (O-2), and O–B and O=C–OH carboxylic groups (O-3), respectively.<sup>42</sup> The high-resolution B 1s peaks (Fig. 1–o) could be deconvoluted into three peaks originating from B–C (190.6 eV), B–N (191.6 eV), and B–O bonds (192.6 eV), respectively.<sup>43</sup> Furthermore, successful doping of B atoms was confirmed by the peaks deconvoluted from the B 1s spectra, corresponding to C–B, N–B, and O–B.

The active heteroatom species N-5, N-6, B-C, and O-1 are the critical species affecting the energy storage performance.<sup>44</sup> The results presented in Table I indicate that the contents of B–C (57.52%) and O-1 (28.10%), and the total content of N-5 (37.43%) and N-6 (20.95%) of UFGC-B-Fe-Zn were higher than in the other samples, facilitating the generation of additional pseudocapacitance at the interface. Moreover, the content of B–N bonds was reduced from 39.65% in UFGC-B to 27.01% and 26.15% in UFGC-B-Fe and UFGC-B-Fe-Zn, demonstrating that some inert B–N bonds were successfully removed by ferric chloride treatment.<sup>45</sup> In

addition, ferric chloride catalyst expedited the formation of active B–C bonds. Thus, UFGC-B-Fe-Zn showed better pseudocapacitance than the other samples, as verified below by the electrochemical performance tests.

The micromorphology of the obtained samples was characterized by SEM (Fig. 3). According to Fig. 3a, the UFGC sample exhibited no highly defective structure, and no obvious pore structure was identified. UFGC-B (Fig. 3b) displayed an obvious pore structure that can be attributed to the interaction between boric acid and carbon atoms resulting in volatilization of volatile compounds during carbonization. In addition, the boron oxides were removed during the subsequent washing. In the SEM image of UFGC-B-Fe (Fig. 3c) more smaller pores can be observed, revealing that the removal of the ferric chloride catalyst by pickling resulted in a more defective structure and more porous structure in the material. In Fig. 3d, a significant defect structure can be identified as well as more disordered pore structures, since zinc chloride can catalyze dehydration while activating. During carbonization, the release of water, carbon dioxide, or other gases successfully achieved pore formation and elevated the degree of defects in the material. The pore structure of UFGC-B-Fe-Zn could provide electron pathways to ensure good contact while also facilitating ion transport by shortening the diffusion paths, thereby improving the electric double-layer capacitance.<sup>46</sup>

Figure 4a illustrates the  $\text{N}_2$  adsorption–desorption isotherms of UFGC, UFGC-B, UFGC-B-Fe, and UFGC-B-Fe-Zn. According to this figure, UFGC exhibited a type IV adsorption/desorption isotherm.<sup>47</sup> The curve hardly rose under relative lower pressure, revealing the existence of significantly few micropores. However, UFGC-B, UFGC-B-Fe, and UFGC-B-Fe-Zn demonstrated a sharply increased type I adsorption–desorption isotherm, suggesting the presence of a texture consisting of many micropores in these samples.<sup>48</sup> Moreover, the curves displayed a distinct hysteresis loop at higher relative pressures, thus revealing the coexistence of abundant meso- and macropores in the carbon framework. These findings are verified by the pore size distribution curves presented in Fig. 4b, demonstrating that UFGC-B, UFGC-B-Fe, and UFGC-B-Fe-Zn contained considerable micropores (0.5 nm to 2 nm) and meso/macropores (2 nm to 252 nm). Table I lists the pore parameters of the samples. In this table, the BET specific surface area ( $S_{\text{BET}}$ ), total pore volume ( $V_{\text{total}}$ ), micropore volume ( $V_{\text{mic}}$ ), and mesopore and macropore volume ( $V_{\text{mec+mac}}$ ) of UFGC were overall low, indicating that there was little pore structure. The increase in  $V_{\text{mec+mac}}$  after boric acid treatment of UFGC resulted from the decomposition of boric acid, and the reaction with carbon in the UFGC mixture during carbonization would release some volatile substances, acting as pore-formers. Besides, the removal of boron oxide

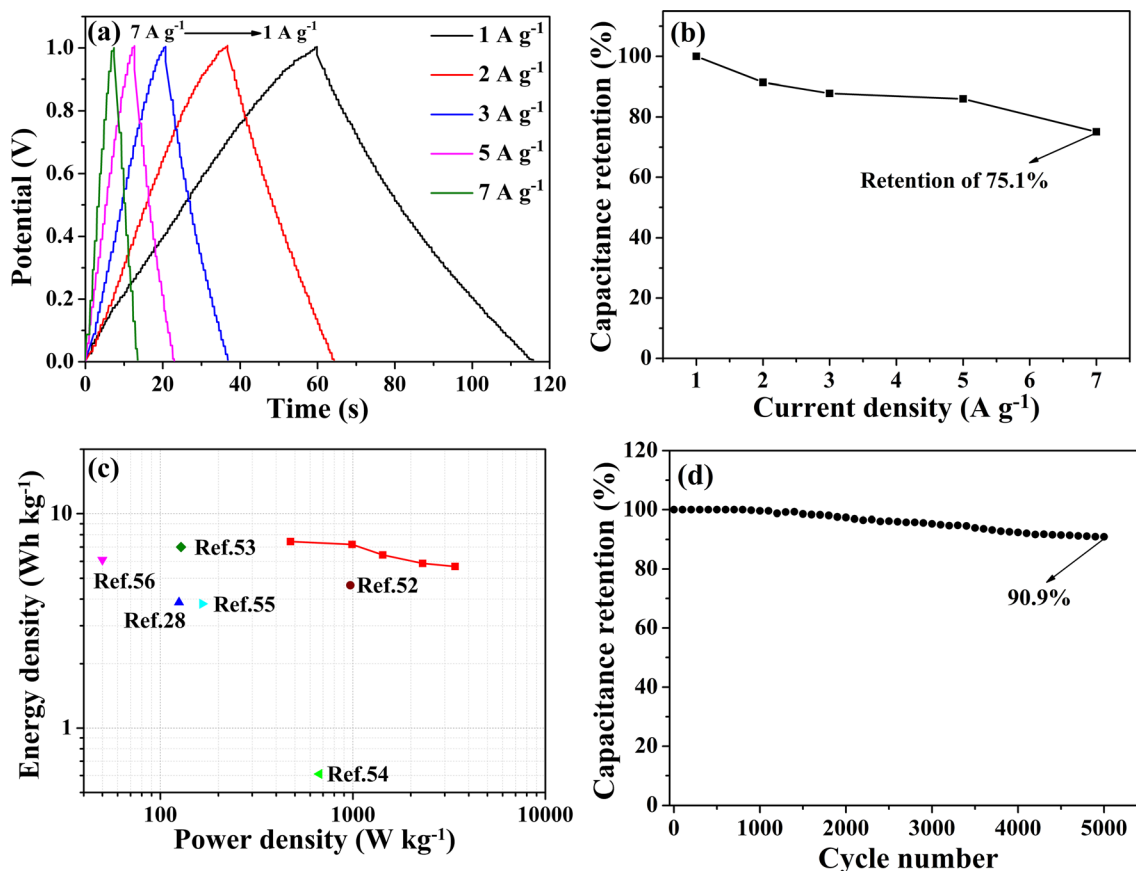


Fig. 6. Electrochemical performance characteristics of UFGC-B-Fe-Zn measured in a symmetrical supercapacitor using 6 M KOH as electrolyte: (a) GCD curves at different current densities from 1 A g<sup>-1</sup> to 7 A g<sup>-1</sup>, (b) capacitance retention at different current densities, (c) Ragone plot of UFGC-B-Fe-Zn symmetrical supercapacitor, and (d) cycling performance at current density of 5 A g<sup>-1</sup>.

during washing was conducive to enriching the pore structure of the material. The  $V_{mic}$  of UFGC-B-Fe was higher than that of UFGC-B, which might be due to the structural defects attributed to pickling to remove the ferric chloride catalyst, and considerable micropores were identified. The results presented in Table I also show that UFGC-B-Fe-Zn exhibited the maximum  $S_{BET}$  (885.9759 m<sup>2</sup> g<sup>-1</sup>),  $V_{mic}$  (0.393158 cm<sup>3</sup> g<sup>-1</sup>), and  $V_{mec} + V_{mac}$  (0.331632 cm<sup>3</sup> g<sup>-1</sup>) values, indicating that activation by zinc chloride could result in the formation of many micropores and mesopores in the samples. The newly formed meso/macropores and micropores in the carbon materials are of great importance to improve the double-layer capacitance and ion diffusion. Moreover, their intermediate specific surface area could improve the contact wettability between the electrode material and electrolyte.<sup>49</sup> Furthermore, the described results reveal that the capacitance of UFGC-B-Fe-Zn originated from pseudocapacitance (generated by heteroatoms) and electrical double-layer capacitance.

The electrochemical performance of the samples was studied systematically using a three-electrode system (Fig. 5) with 6 M KOH aqueous solution as electrolyte. Figure 5a shows the CV curves of all the materials obtained at a scanning rate of 5 mV s<sup>-1</sup>,

indicating a slightly deformed rectangular shape. Except for UFGC, the CV curves of the other samples overall showed humps, showing that their capacitance behavior consisted of electrical double-layer capacitance and pseudocapacitance generated from N, B, and O heteroatoms in the carbon skeleton. The CV curves suggest that the integral area of the UFGC-B-Fe-Zn was the widest, indicating the optimal capacitance. The CV curves of UFGC-B-Fe-Zn obtained at different scanning rates of 1 mV s<sup>-1</sup>, 5 mV s<sup>-1</sup>, 10 mV s<sup>-1</sup>, 20 mV s<sup>-1</sup>, 50 mV s<sup>-1</sup>, 100 mV s<sup>-1</sup>, and 200 mV s<sup>-1</sup> are plotted in Fig. 5b. The CV curves remain rectangular without significant deformation at the scanning rate of 100 mV s<sup>-1</sup>, showing stable rate performance. To prove the pseudocapacitance effect of heteroatoms, UFGC-B-Fe-Zn-900 was prepared from UFGC-B-Fe-Zn by heat treatment under N<sub>2</sub> at 900°C for 2 h to remove heteroatoms. The XPS survey spectrum of UFGC-B-Fe-Zn-900 (Fig. 1q) shows that most of the heteroatoms had been removed at high temperature. Figure 4c shows the CV curve of UFGC-B-Fe-Zn-900. After high-temperature treatment, the CV curve of UFGC-B-Fe-Zn-900 displayed a more regular, narrower rectangle with no obvious peaks, indicating that the partial capacitance of UFGC-B-Fe-Zn was contributed by heteroatoms.

To further confirm the capacitance performance of UFGC, UFGC-B, UFGC-B-Fe, and UFGC-B-Fe-Zn, GCD tests were performed. Figure 5d shows the GCD test curves of the four samples at a current density of  $0.5 \text{ A g}^{-1}$ , revealing overall a marginally deformed symmetric triangle shape. As shown by the GCD test curves of UFGC-B-Fe-Zn obtained at various current densities (Fig. 5e), the charging and discharging times gradually shortened with improvement of the current density, corresponding to a decrease in the specific capacitance. This occurred because, when charging or discharging under high current density, electrolyte ions failed to permeate the microporous structure of the material in a timely fashion, so the electrode material could not be thoroughly exploited. No significant voltage drop was observed in the GCD curves, verifying that, due to the good electrode–electrolyte interfacial contact, the internal resistance was low, which is conducive to high power transmission. At a current density of  $0.5 \text{ A g}^{-1}$ , the specific capacitance of the UFGC-B-Fe-Zn electrode reached  $377.4 \text{ F g}^{-1}$ . Moreover, the capacitance reached  $263.8 \text{ F g}^{-1}$  at the high current density of  $7 \text{ A g}^{-1}$ . The capacitance retention rate reached 70%, indicating excellent rate performance. UFGC-B-Fe-Zn exhibited performance that was better than or similar to samples of an identical type reported in previous literature.

In addition, EIS is one of the techniques used to explore the electrochemical behavior of samples. Figure 5g shows the Nyquist plots of UFGC, UFGC-B, UFGC-B-Fe, and UFGC-B-Fe-Zn, comprising in each case a semicircle in the high-frequency range and a slope line in the low-frequency range.<sup>50</sup> Figure 5h shows a corresponding equivalent circuit model. The intercept of the curve with the  $x$ -axis occurs at  $R_s$ , corresponding to the bulk solution resistance. According to the results presented in Table II, all the samples showed significantly low  $R_s$  values, indicating a short electron path length and low electrolyte resistance. The diameter of the semicircle closely represents the charge-transfer resistance ( $R_{ct}$ ); the smaller the  $R_{ct}$  value of the sample, the more conducive to charge transfer it will be, and the better its electrochemical activity. The high slope of the low-frequency straight line indicates rapid diffusion and transmission of ions; the smaller the value of  $W_R$ , the faster the electrolyte ion diffusion rate will be. Table II shows that the  $R_s$ ,  $R_{ct}$ , and  $W_R$  values of UFGC-B-Fe-Zn were the minimum, reaching  $0.43897 \text{ } \Omega$ ,  $0.75662 \text{ } \Omega$ , and  $1.088$ , respectively. In summary, these results indicate that UFGC-B-Fe-Zn exhibited high electrical conductivity, fast charge transfer, and electrolyte ion pervasion, accounting for its excellent electrochemical performance.<sup>51</sup>

Figure 5i shows the CV curves of UFGC-B-Fe-Zn in the 1st and 3000th cycle, revealing little change. Moreover, Fig. 4j shows that the capacitance retention rate of UFGC-B-Fe-Zn in the 3000th cycles was

up to 95.1%, demonstrating that UFGC-B-Fe-Zn exhibited excellent electrochemical stability and cycling life.

To assess the supercapacitor performance of UFGC-B-Fe-Zn in the potential window of 1 V, a UFGC-B-Fe-Zn//UFGC-B-Fe-Zn symmetrical supercapacitor was assembled to carry out electrochemical testing on a two-electrode system (Fig. 6). Figure 6a shows the GCD curves of the UFGC-B-Fe-Zn//UFGC-B-Fe-Zn supercapacitor at different current densities. The GCD curves show a symmetrical triangular shape with slight deformation, indicating pseudocapacitance behavior during charging and discharging. Moreover, the curves show a low voltage drop, verifying the excellent capacitive behavior of the UFGC-B-Fe-Zn //UFGC-B-Fe-Zn supercapacitor. At a current density of  $1 \text{ A g}^{-1}$ , the specific capacitance reached  $57.84 \text{ F g}^{-1}$ , it remained at  $43.42 \text{ F g}^{-1}$  under a high current density of  $7 \text{ A g}^{-1}$ , with a capacitance retention rate of 75.1% (Fig. 6b). These results thus demonstrate that the UFGC-B-Fe-Zn//UFGC-B-Fe-Zn supercapacitor exhibited excellent rate performance. The Ragone diagram of the UFGC-B-Fe-Zn//UFGC-B-Fe-Zn supercapacitor is presented in Fig. 5c. The energy density reached  $7.43 \text{ Wh kg}^{-1}$  at a power density of  $474 \text{ W kg}^{-1}$ . Furthermore, the energy density reached  $5.68 \text{ Wh kg}^{-1}$  at a power density of  $3396 \text{ W kg}^{-1}$ . The performance was better than that of previously reported B-doped graphene material ( $3.86 \text{ Wh kg}^{-1}$  and  $125 \text{ W kg}^{-1}$ ,<sup>28</sup>  $4.64 \text{ Wh kg}^{-1}$  and  $970 \text{ W kg}^{-1}$ ),<sup>52</sup> graphene-based materials ( $7.0 \text{ Wh kg}^{-1}$  and  $128 \text{ W kg}^{-1}$ ,<sup>53</sup>  $0.61 \text{ Wh kg}^{-1}$  and  $670 \text{ W kg}^{-1}$ ),<sup>54</sup> B-doped carbon ( $3.8 \text{ Wh kg}^{-1}$  and  $165 \text{ W kg}^{-1}$ ),<sup>55</sup> and carbon material activated by zinc chloride ( $6.1 \text{ Wh kg}^{-1}$  and  $50 \text{ W kg}^{-1}$ ).<sup>56</sup> The capacitance retention rate of the UFGC-B-Fe-Zn//UFGC-B-Fe-Zn supercapacitor was up to 90.9% after 5000 charge–discharge cycles, demonstrating its good cycling stability. Accordingly, the results described above prove that UFGC-B-Fe-Zn represents an excellent energy storage electrode material based on zinc-chloride-activated heteroatom-doped carbon.

## CONCLUSION

Carbon powder materials were successfully prepared by using graphene oxide synthesized from mineral graphite and common polymers as raw materials, thereby demonstrating a more viable method for the development of high-capacitance carbon powder materials for supercapacitor electrodes. The polyurethane/phenolic/graphene oxide composite material treated with boric acid, ferric chloride, and zinc chloride could be carbonized by using a one-step carbonization method. Moreover, after washing the carbon powder material with hydrochloric acid and water, high-specific-capacitance B-doped carbon powder material with intermediate specific surface area and porosity could be

successfully synthesized. While boric acid provided the carbon powder materials with B heteroatoms, it also increased the pore structure of the materials. Ferric chloride as a catalyst could efficiently hinder formation of inert B–N bonds and improve the pseudocapacitance behavior of the material. Zinc chloride as an activator could effectively increase the  $S_{\text{BET}}$  value of the material and optimize its pore structure. The  $S_{\text{BET}}$  of UFGC-B-Fe-Zn was 5.7 times that of UFGC, reaching  $885.9759 \text{ m}^2 \text{ g}^{-1}$ . A maximum specific capacitance value of  $377.4 \text{ F g}^{-1}$  at  $0.5 \text{ A g}^{-1}$  was achieved with UFGC-B-Fe-Zn. It also exhibited both excellent rate performance and cycling stability over 3000 cycles (95.1%). A high energy density of  $7.43 \text{ Wh kg}^{-1}$  was reached at  $474 \text{ W kg}^{-1}$  for an UFGC-B-Fe-Zn/UFGC-B-Fe-Zn symmetrical supercapacitor. Furthermore, it exhibited an excellent capacitance retention rate of 90.9% over 5000 cycles.

### ACKNOWLEDGEMENTS

The authors are grateful for the support of the National Natural Science Foundation of China (Grant No. 21372067) and the Joint Guidance Project of Natural Science Foundation of Heilongjiang Province (Grant No. LH2020E103).

### CONFLICT OF INTEREST

The authors declare that they have no conflicts of interest.

### REFERENCES

- S. Demirezen, A. Kaya, S.A. Yerişkin, M. Balbaşı, and İ Uslu, S. Demirezen, A. Kaya, S.A. Yerişkin, M. Balbaşı, and İ Uslu, *Res. Phys.* 6, 180–185 (2016).
- J.L. Zheng, X. Pan, X.M. Huang, D.B. Xiong, Y. Shang, X.X. Li, N. Wang, W.M. Lau, and H.Y. Yang, J.L. Zheng, X. Pan, X.M. Huang, D.B. Xiong, Y. Shang, X.X. Li, N. Wang, W.M. Lau, and H.Y. Yang, *Chem. Eng. J.* 396, 125197 (2020).
- N.L.W. Septiani, Y.V. Kaneti, K.B. Fathoni, J. Wang, Y. Ide, B. Yuliarto, Nugraha, H.K. Dipojono, A.K. Nanjundan, D. Golberg, Y. Bando, and Y. Yamauchi, N.L.W. Septiani, Y.V. Kaneti, K.B. Fathoni, J. Wang, Y. Ide, B. Yuliarto, Nugraha, H.K. Dipojono, A.K. Nanjundan, D. Golberg, Y. Bando, and Y. Yamauchi, *Nano Energy* 67, 104270 (2020).
- S. Satpathy, S. Das, and B.K. Bhattacharyya, S. Satpathy, S. Das, and B.K. Bhattacharyya, *J. Energy Storage* 27, 101044 (2020).
- Q. Miao, F. Rouhani, H. Moghanni-Bavil-Olyaei, K.G. Liu, X.M. Gao, J.Z. Li, X.D. Hu, Z.M. Jin, M.L. Hu, and A. Morsali, Q. Miao, F. Rouhani, H. Moghanni-Bavil-Olyaei, K.G. Liu, X.M. Gao, J.Z. Li, X.D. Hu, Z.M. Jin, M.L. Hu, and A. Morsali, *Chem. Eur. J.* 10, 1002 (2020).
- J.H. Jiang, W.D. Shi, S.Y. Song, Q.L. Hao, W.Q. Fan, X.F. Xia, X. Zhang, Q. Wang, and D. Yan, J.H. Jiang, W.D. Shi, S.Y. Song, Q.L. Hao, W.Q. Fan, X.F. Xia, X. Zhang, Q. Wang, and D. Yan, *J. Power Sources* 248, 1281 (2014).
- Q. Abbas, and F. Béguin, Q. Abbas, and F. Béguin, *Prog. Nat. Sci.* 25, 622 (2015).
- H. Sun, P. She, K.L. Xu, Y.X. Shang, S.Y. Yin, and Z.N. Liu, H. Sun, P. She, K.L. Xu, Y.X. Shang, S.Y. Yin, and Z.N. Liu, *Synth. Met.* 209, 68 (2015).
- M. Mohan, K.N.N. Unni, and R.B. Rakhi, M. Mohan, K.N.N. Unni, and R.B. Rakhi, *Vacuum* 166, 335 (2019).
- D. Shao, L. Wang, B. Lu, J. Guo, S. Zhang, and Y. Lu, D. Shao, L. Wang, B. Lu, J. Guo, S. Zhang, and Y. Lu, *J. Electroanal. Chem.* 847, 113188 (2019).
- Z.G. Özdemir, N.Y. Canli, B. Senkal, Y. Gürsel, and M. Okutan, Z.G. Özdemir, N.Y. Canli, B. Senkal, Y. Gürsel, and M. Okutan, *J. Mol. Liq.* 211, 442 (2015).
- J. Huo, P. Zheng, X. Wang, and S. Guo, J. Huo, P. Zheng, X. Wang, and S. Guo, *Appl. Surf. Sci.* 442, 575 (2018).
- K.V. Karthik, N.S. Shruthi, V. Ganagaraju, and D. Rangappa, K.V. Karthik, N.S. Shruthi, V. Ganagaraju, and D. Rangappa, *Mater. Today Proc.* 4, 12229–12237 (2017).
- L. Sun, H. Zhou, L. Li, Y. Yao, H.N. Qu, C.L. Zhang, S.H. Liu, and Y.M. Zhou, L. Sun, H. Zhou, L. Li, Y. Yao, H.N. Qu, C.L. Zhang, S.H. Liu, and Y.M. Zhou, *ACS Appl. Mater. Interfaces* 9, 26088 (2007).
- F.Y. Ke, J. Tang, S.Y. Guang, and H.Y. Xu, F.Y. Ke, J. Tang, S.Y. Guang, and H.Y. Xu, *RSC Adv.* 6, 14712 (2016).
- T. Eguchi, D. Tashima, M. Fukuma, and S. Kumagai, T. Eguchi, D. Tashima, M. Fukuma, and S. Kumagai, *J. Clean Prod.* 259, 120822 (2020).
- X. Zhang, Y. Wang, Y. Du, M. Qing, F. Yu, Z.Q. Tian, and P.K. Shen, X. Zhang, Y. Wang, Y. Du, M. Qing, F. Yu, Z.Q. Tian, and P.K. Shen, *Electrochim. Acta* 20, 272 (2019).
- A. Kurniawan, L.K. Ong, F. Kurniawan, C.X. Lin, F.E. Soetaredjo, X.S. Zhao, and S. Ismadji, A. Kurniawan, L.K. Ong, F. Kurniawan, C.X. Lin, F.E. Soetaredjo, X.S. Zhao, and S. Ismadji, *RSC Adv.* 4, 34739 (2014).
- L. Sun, H. Zhou, Y. Li, F. Yu, C. Zhang, X. Liu, and Y. Zhou, L. Sun, H. Zhou, Y. Li, F. Yu, C. Zhang, X. Liu, and Y. Zhou, *Mater. Lett.* 189, 107 (2017).
- P. Wang, G. Zhang, M.Y. Li, Y.X. Yin, J.Y. Li, G. Li, W.P. Wang, P. Wen, F.F. Cao, and Y.G. Guo, P. Wang, G. Zhang, M.Y. Li, Y.X. Yin, J.Y. Li, G. Li, W.P. Wang, P. Wen, F.F. Cao, and Y.G. Guo, *Chem. Eng. J.* 375, 122020 (2019).
- L. Sun, Y. Yao, Y. Zhou, L. Li, H. Zhou, M. Guo, S. Liu, C. Feng, Z. Qi, B. Gao, and A.C.S. Sustain, L. Sun, Y. Yao, Y. Zhou, L. Li, H. Zhou, M. Guo, S. Liu, C. Feng, Z. Qi, B. Gao, and A.C.S. Sustain, *Chem. Eng.* 6, 13494 (2018).
- X.L. Dong, A.H. Lu, B. He, and W.C. Li, X.L. Dong, A.H. Lu, B. He, and W.C. Li, *J. Power Sources* 327, 535 (2016).
- H. Sun, H. Quan, M. Pan, Z. Zhang, Y. Zeng, and D. Chen, H. Sun, H. Quan, M. Pan, Z. Zhang, Y. Zeng, and D. Chen, *J. Alloys Compd.* 826, 154208 (2020).
- H. Lin, Y. Liu, Z. Chang, S. Yan, S. Liu, and S. Han, H. Lin, Y. Liu, Z. Chang, S. Yan, S. Liu, and S. Han, *Microporous Mesoporous Mater.* 292, 109707 (2020).
- M. Hãrmas, T. Thomberg, H. Kurig, T. Romann, A. Jãnes, and E. Lust, M. Hãrmas, T. Thomberg, H. Kurig, T. Romann, A. Jãnes, and E. Lust, *J. Power Sources* 326, 624 (2016).
- M. Hãrmas, T. Thomberg, and A. Jãnes, M. Hãrmas, T. Thomberg, and A. Jãnes, *J. Electrochem. Soc.* 167, 080533 (2020).
- S.S. Balaji, M. Karnan, P. Anandhaganesh, S.M. Tauquir, and M. Sathish, S.S. Balaji, M. Karnan, P. Anandhaganesh, S.M. Tauquir, and M. Sathish, *Appl. Surf. Sci.* 491, 560 (2019).
- L. Niu, Z. Li, W. Hong, J. Sun, Z. Wang, L. Ma, J. Wang, and S. Yang, L. Niu, Z. Li, W. Hong, J. Sun, Z. Wang, L. Ma, J. Wang, and S. Yang, *Electrochim. Acta.* 108, 666 (2013).
- J. Li, X. Li, D. Xiong, L. Wang, and D. Li, J. Li, X. Li, D. Xiong, L. Wang, and D. Li, *Appl. Surf. Sci.* 475, 285 (2019).
- J. Gao, X. Wang, Y. Zhang, J. Liu, Q. Lu, and M. Liu, J. Gao, X. Wang, Y. Zhang, J. Liu, Q. Lu, and M. Liu, *Electrochim. Acta.* 207, 266 (2016).
- R. Nankya, J. Lee, D.O. Opar, and H. Jung, R. Nankya, J. Lee, D.O. Opar, and H. Jung, *Appl. Surf. Sci.* 489, 552 (2019).
- L.K. Shrestha, R.G. Shrestha, S. Maji, B.P. Pokharel, R. Rajbhandari, R.L. Shrestha, R.R. Pradhananga, J.P. Hill, and K. Ariga, L.K. Shrestha, R.G. Shrestha, S. Maji, B.P. Pokharel, R. Rajbhandari, R.L. Shrestha, R.R. Prad-

- hananga, J.P. Hill, and K. Ariga, *Nanomaterials*. 10, 728 (2020).
33. J. Li, F. Luo, T. Lin, J. Yang, S. Yang, D. He, D. Xiao, and W. Liu, J. Li, F. Luo, T. Lin, J. Yang, S. Yang, D. He, D. Xiao, and W. Liu, *Chem. Phys. Lett.* 753, 137597 (2020).
  34. R.L. Shrestha, T. Shrestha, B.M. Tamrakar, R.G. Shrestha, S. Maji, K. Ariga, and L.K. Shrestha, R.L. Shrestha, T. Shrestha, B.M. Tamrakar, R.G. Shrestha, S. Maji, K. Ariga, and L.K. Shrestha, *Materials*. 13, 2371 (2020).
  35. W.S. Hummers, R.E. Offeman, and J. Am, W.S. Hummers, and R.E. Offeman, *J. Am. Chem. Soc.* 80, 1339 (1985).
  36. R. Yan, K. Leus, J.P. Hofmann, M. Antonietti, and M. Oschatz, R. Yan, K. Leus, J.P. Hofmann, M. Antonietti, and M. Oschatz, *Nano Energy*. 67, 104240 (2020).
  37. Z. Chen, L. Hou, Y. Cao, Y. Tang, and Y. Li, Z. Chen, L. Hou, Y. Cao, Y. Tang, and Y. Li, *Appl. Surf. Sci.* 435, 937 (2018).
  38. J.L.G. Urbano, G.M. Fernandez, M. Arnaiz, J. Ajuria, T. Rojo, and D. Carriazo, J.L.G. Urbano, G.M. Fernandez, M. Arnaiz, J. Ajuria, T. Rojo, and D. Carriazo, *Carbon* 162, 273 (2020).
  39. B. Ashourirad, M. Demir, R.A. Smith, R.B. Gupta, and H.M. El-Kaderi, B. Ashourirad, M. Demir, R.A. Smith, R.B. Gupta, and H.M. El-Kaderi, *RSC Adv.* 8, 12300 (2018).
  40. H. Jia, S. Qiu, W. Li, D. Liu, and X. Xie, H. Jia, S. Qiu, W. Li, D. Liu, and X. Xie, *J. Electroanal. Chem.* 863, 114057 (2020).
  41. K. Zeng, J. Su, X. Cao, X. Zheng, X. Li, J.H. Tian, C. Jin, and R. Yang, K. Zeng, J. Su, X. Cao, X. Zheng, X. Li, J.H. Tian, C. Jin, and R. Yang, *J. Alloys Compd.* 824, 153908 (2020).
  42. X. Hu, Y. Deng, J. Zhou, B. Liu, A. Yang, T. Jin, and Y.F. Tsang, X. Hu, Y. Deng, J. Zhou, B. Liu, A. Yang, T. Jin, and Y.F. Tsang, *Sep. Purif. Technol.* 251, 117376 (2020).
  43. Y. Chang, C. Yuan, C. Liu, J. Mao, Y. Li, H. Wu, Y. Wu, Y. Xu, B. Zeng, and L. Dai, Y. Chang, C. Yuan, C. Liu, J. Mao, Y. Li, H. Wu, Y. Wu, Y. Xu, B. Zeng, and L. Dai, *J. Power Sources*. 365, 354 (2017).
  44. Y. Ma, X. Zhang, Z. Liang, C. Wang, Y. Sui, B. Zheng, Y. Ye, W. Ma, Q. Zhao, and C. Qin, Y. Ma, X. Zhang, Z. Liang, C. Wang, Y. Sui, B. Zheng, Y. Ye, W. Ma, Q. Zhao, and C. Qin, *Electrochim. Acta*. 337, 135800 (2020).
  45. C. Wang, X. Zhang, J. Wang, Y. Ma, S. Lv, J. Xiang, M. Chu, T. Sun, and C. Qin, C. Wang, X. Zhang, J. Wang, Y. Ma, S. Lv, J. Xiang, M. Chu, T. Sun, and C. Qin, *J. Electrochem. Soc.* 165, A1 (2018).
  46. Y. Liang, Y. Lu, G. Xiao, J. Zhang, H. Chi, and Y. Dong, Y. Liang, Y. Lu, G. Xiao, J. Zhang, H. Chi, and Y. Dong, *Appl. Surf. Sci.* 529, 147141 (2020).
  47. F. Wang, L. Chen, H. Li, G. Duan, S. He, L. Zhang, G. Zhang, Z. Zhou, and S. Jiang, F. Wang, L. Chen, H. Li, G. Duan, S. He, L. Zhang, G. Zhang, Z. Zhou, and S. Jiang, *Chin. Chem. Lett.* 31, 1986 (2020).
  48. B. Yu, G. Jiang, C. Cao, N. Lei, C. Li, U. Evariste, and P. Ma, B. Yu, G. Jiang, C. Cao, N. Lei, C. Li, U. Evariste, and P. Ma, *J. Energy Storage*. 30, 101537 (2020).
  49. S.A. Ansari, N. Parveen, H.M. Kotb, and A. Alshoabi, S.A. Ansari, N. Parveen, H.M. Kotb, and A. Alshoabi, *Electrochim. Acta*. 355, 136783 (2020).
  50. Y. Huang, J. Yang, L. Hu, D. Xia, Q. Zhang, Y. Liao, H. Li, W. Yang, C. He, and D. Shu, Y. Huang, J. Yang, L. Hu, D. Xia, Q. Zhang, Y. Liao, H. Li, W. Yang, C. He, and D. Shu, *Environ. Sci. NANO* 6, 1430 (2019).
  51. Z. Gao, X. Wang, J. Chang, D. Wu, L. Wang, X. Liu, F. Xu, Y. Guo, and K. Jiang, Z. Gao, X. Wang, J. Chang, D. Wu, L. Wang, X. Liu, F. Xu, Y. Guo, and K. Jiang, *RSC Adv.* 5, 48665 (2015).
  52. V. Thirumal, A. Pandurangan, R. Jayavel, and R. Ilangoan, V. Thirumal, A. Pandurangan, R. Jayavel, and R. Ilangoan, *Synth. Met.* 220, 524 (2016).
  53. M. Wang, J. Yang, S. Liu, M. Li, C. Hu, and J. Qiu, M. Wang, J. Yang, S. Liu, M. Li, C. Hu, and J. Qiu, *J. Colloid Interface Sci.* 560, 69 (2020).
  54. Y. Xu, Z. Lin, X. Huang, Y. Liu, Y. Huang, and X. Duan, Y. Xu, Z. Lin, X. Huang, Y. Liu, Y. Huang, and X. Duan, *ACE NANO*. 7, 4042 (2013).
  55. H. Guo, and Q. Gao, H. Guo, and Q. Gao, *J. Power Sources*. 186, 551 (2009).
  56. C. Wang, and T. Liu, C. Wang, and T. Liu, *J. Alloys Compd.* 696, 42 (2017).

**Publisher's Note** Springer Nature remains neutral with regard to jurisdictional claims in published maps and institutional affiliations.